Fall 2016

Development and testing of a fracture energy-based model of explosive asteroid deflection

James A. Veerkamp

Department:

DEVELOPMENT AND TESTING OF A FRACTURE ENERGY-BASED MODEL OF EXPLOSIVE ASTEROID DEFLECTION

by

JAMES A. VEERKAMP

A THESIS

Presented to the Faculty of the Graduate School of the

MISSOURI UNIVERSITY OF SCIENCE AND TECHNOLOGY

In Partial Fulfillment of the Requirements for the Degree

MASTER OF SCIENCE IN AEROSPACE ENGINEERING

2016

Approved by

Henry J. Pernicka, Co-Advisor
Leslie S. Gertsch, Co-Advisor
Kyle J. DeMars

ABSTRACT

While asteroid deflection has been studied for the past half century, efforts have generally been directed towards methods that attempt to minimize disruption of the rock body. In order to widen the base of research, a fracture energy-based model of asteroid fragmentation was developed and applied to both asteroid scale and lab testable scale cases. Modeling of the orbital case suggests the capability to deflect a 100 meter diameter asteroid on a 10 year timescale. The model's predicted energy transfer is then compared to laboratory testing using a ballistic pendulum. The results of this testing suggest that the model as described overestimates the efficiency of energy transfer into momentum. However, further approaches are suggested that might improve model accuracy as well as energy transfer efficiency.

ACKNOWLEDGMENTS

Special thanks are owed to Dr. Pernicka, for teaching me almost everything I know about orbital dynamics, and for being the most consistently supportive figure in my undergraduate and graduate terms, even when I went astray. I came to him with a crazy idea for interdisciplinary studies, and I could have never made it this far without his help.

Thanks also go to Dr. Gertsch, who has somehow managed to teach me more about rocks floating in space in three years than I ever thought possible, and whose enthusiasm for this research has proved infectious. Also for procuring funds for testing. That definitely helped too.

Additional thanks to Dr. DeMars for graciously agreeing to join my committee, and for offering aid in the selection of test procedure early on, which led into our ballistic pendulum testing.

Finally, thanks are due to the family and friends who have supported me through this process, as well as all the other unmentioned professors who have taught me so much over the years. This wouldn’t have been possible without everyone’s support.

TABLE OF CONTENTS

LIST OF ILLUSTRATIONS

Page

LIST OF TABLES

Page

1. INTRODUCTION

1.1. PROBLEM STATEMENT

Current literature on asteroid deflection methods contains a wide variety of possible methods for deflecting asteroids. However, the vast majority of analyses neglect classes of deflection methods that might induce breakup of some portion of the asteroid. While these methods run the risk of creating a cloud of debris, some portion of which could impact the Earth, the increased energy applied to the main body could in principle allow for an asteroid to be deflected closer to the date of impact than non-fragmentary methods. This is of use in cases where an impacting body may not be discovered with the multiple decades of warning necessary to implement other methods of asteroid deflection. The development and testing of a model of the fracture energy dynamics governing the partial fracturing of an asteroid can suggest further research into explosive asteroid deflection possibilities.

1.2. ASSUMED KNOWLEDGE

In the preparation of this thesis, it has been assumed that the reader has a basic understanding of orbital dynamics. In particular, basic two body problem mechanics, as well as the Tsiolkovsky rocket equation governing velocity change under thrust is essential to understand the model as developed. Additionally, an understanding of computational modeling techniques and methods will generally aid comprehension throughout the work. A limited amount of rock fracture mechanics is covered, but lack of prior understanding should not impede comprehension of the work. A brief review of some topics is provided, but the reader should refer to other sources, particularly those referenced in the literature overview, for a more in-depth discussion of these subjects.

2. LITERATURE REVIEW

Since the publication of the first semi-serious consideration of changing an asteroid's orbit by Dandridge M. Cole in 1964 [1], asteroid deflection has held a slowly growing place within scientific literature. The process was initially considered as a means of capturing an asteroid into Earth orbit for the purposes of mining and settlement. However, after the publication in 1980 of research by Luis and Walter Alvarez implicating a large asteroid collision in the extinction of the dinosaurs [2], the pace of research increased as a response to the threat of asteroid impact.

The pace of research increased through the 1980s and into the early 90s, as the NASA Spaceguard asteroid search program began publishing results [3], as well as multiple workshops on the topic [4,5] held by NASA. One of the most comprehensive papers from the time is Ahrens' and Harris' "Deflection and fragmentation of near-Earth asteroids" published in Nature in 1992 [6]. Covering standoff nuclear deflection, kinetic interceptors, as well as mass drivers and whole body fragmentation approaches, the paper still serves as an excellent summary of the more aggressive methods of asteroid deflection.

Along with these more aggressive methods of asteroid deflection, in recent years much work has been dedicated to studying less disruptive but slower acting means of deflection. Edward Lu described a method of using a spacecraft gravitationally bound to an asteroid while supplying small amounts of thrust via ion engines as a means of deflecting an asteroid without ever coming into direct contact with the body [7]. Along a similar vein, C. Bombardelli suggested use of exhaust from the ion thrusters of an orbiting spacecraft impinging on the surface of an asteroid to create a drag force on the body [8]. However, in a 2007 NASA review, the near term utility of these approaches was questioned, due to their necessitating multi-decadal mission lengths and requiring unprecedentedly high spacecraft reliability [9].

In addition to recent research into nondisruptive deflection methods, there has been some exceptional work researching combined hypervelocity impactors and nuclear explosives recently in literature by Bong Wie and Brent Barbee and the Asteroid Deflection Research Center at Iowa State [10]. The proposed mission combines aspects

of multiple different classes of mission. A lead impactor would excavate a shallow surface crater, with a follow-up payload bus delivering a nuclear explosive to detonate within the crater, improving the thrusting efficiency over standoff and surface nuclear detonations. Of the many approaches under research, a combined mission design such as this might hold the greatest promise for the future of asteroid defense.

In the study of fracture mechanics of brittle materials, all roads lead to A. A. Griffiths' work in the 1920s [11]. His work focused on the fracture behavior of brittle solids, and was based around the interplay between strain energy and the free surface energy of cracked surfaces. This work continues to inform modern fracture analyses, with additional refinements to the method coming from Irwin and others in the 1950s [12].

Unfortunately, very little published research exists governing the fracture properties of asteroid material. There is some research studying the dynamic response of chondritic material that suggests a path forward to approximating the key values. Kimberley's work in 2011 gives measured values for Young's Modulus of an ordinary chondrite [13]. However, the critical stress intensity value is not measured, and is only assumed to be lower by some unspecified factor than a loosely equivalent terrestrial rock. This dearth of information does not ease the construction of a fracture energy model of asteroid deflection.

3. DEVELOPMENT OF INITIAL MODEL

3.1. BASIC ASSUMPTIONS

In order to develop a model for the deflection induced by an explosive fracturing of an asteroid, certain assumptions and simplifications are made, as follows:

- The physical parameters of the asteroid must be known and well-characterized, specifically the geometry, density, and fracture energy of the constituent material.
- The geometry of the fractured portion of the asteroid must be estimable, and some means of approximating the area generated by fracturing need be chosen
- The energy to fracture the newly generated area must scale linearly with the area produced. This generally follows under Griffith's criterion in fracture mechanics.
- The post-blast behavior of the ejecta must be well-characterized.
- Any thrust generated will act through the asteroid center of mass, minimizing any loss of energy to rotational motion.

In addition, the mass of any explosives, and the gases produced by explosives have been neglected as insignificant relative to the asteroid as a whole. Accounting for these simplifications, a model for the deflection of an asteroid that has been explosively fractured can be developed using energy-based methods.

3.2. MODEL CONSTRUCTION

In order to develop the model, start by determining the volume and mass of the asteroid. If the asteroid is uniform and spherical, for demonstration purposes, the volume and mass can be determined from the radius $r_{Asteroid}$ and the density ρ as

$$V_{Asteroid} = \frac{4}{3}\pi {r_{Asteroid}}^3 \quad (1)$$

$$M_{Asteroid} = \rho V_{Asteroid} \quad (2)$$

Then, the fractured volume of the asteroid and the new surface area generated through fracturing must be estimated. For geometric simplicity, a spherical cap section has been assumed. The volume of a spherical cap is given by the following equation, where *h* is the depth of the spherical cap as shown in Figure 3.1.

$$V_{Fractured} = \frac{\pi h^2}{3}(3r_{asteroid} - h) \quad (3)$$

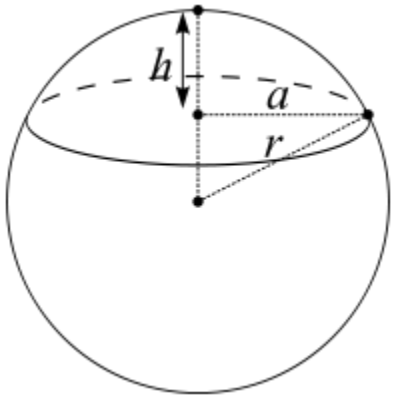

Figure 3.1. Geometry of a Spherical Cap

The area produced from fracturing can then be approximated at a rough upper bound by calculating the surface area of a group of small spherical fragments of equal volume to the original fractured volume. The process for this is

$$v_{fragment} = \frac{4}{3}\pi {r_{fragment}}^3 \quad (4)$$

$$a_{fragment} = 4\pi {r_{fragment}}^2 \quad (5)$$

$$n_{Fragments} = \frac{V_{Fractured}}{v_{fragment}} \quad (6)$$

$$A_{Fractured} = n_{Fragments} a_{fragment} \quad (7)$$

While this condition neglects the original area of the free surface of the asteroid, for any fracturing event where many small fragments are created, the area produced through fracturing will be much larger than the original free surface, and so is solely considered in this approach to modeling asteroid fracturing.

The energy necessary for fracturing the asteroid must then be subtracted from the total explosive energy.

$$E_{Fracture} = A_{Fractured} \gamma_{wof} \quad (8)$$

$$E_{Remainder} = E_{Explosive} - E_{Fracture} \quad (9)$$

In these equations γ_{wof} is the work of fracture, the energy necessary to create a unit area of new surface. If the quantity $E_{Remainder}$ is negative, the explosive energy would be insufficient to fracture the modeled fractured region, and analysis can be halted there. However, if the remainder is positive, the energy must then be apportioned to the main body and the remaining fragments. The geometry before and after detonation can be seen in Figure 3.2.

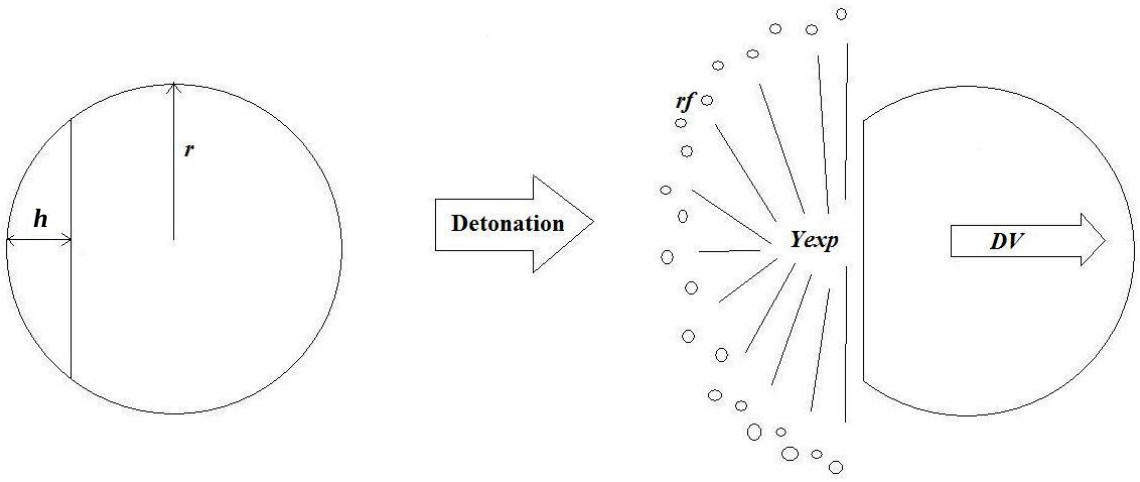

Figure 3.2. System Geometry Pre- and Post-Detonation

The apportionment of this energy between the main body and the fragments is somewhat complex and requires the construction of a system of equations that can be simultaneously solved for both values. Development of that system starts from the energy balance.

$$E_{Remainder} = n_{fragments}E_{fragment} + E_{main} \quad (10)$$

As a secondary condition, the change in velocity of the main body should agree with the velocity change predicted by the Tsiolkovsky rocket equation

$$\Delta V_{main} = V_{exhaust} \ln\left(\frac{M_{Asteroid}}{M_{main}}\right) \quad (11)$$

where $V_{exhaust}$ is the effective average velocity component of the fragments created in the direction of net thrust, and M_{main} is the mass of the asteroid minus the total mass of fragments ejected ($n_{fragments}\rho v_{fragment}$).

If equation (10) is rewritten in terms of velocities, and the exhaust velocity is expressed as some constant $\alpha \leq 1$ times the fragment velocity, the system of equations in terms of velocities is of the following form:

$$E_{Remainder} = \frac{1}{2}M_{main}(\Delta V_{main})^2 + \frac{n_{fragments}}{2}m_{fragment}(V_{fragment})^2 \quad (12)$$

$$\Delta V_{main} = \alpha V_{fragment} \ln\left(\frac{M_{Asteroid}}{M_{main}}\right) \quad (13)$$

In the above system of equations, the term $m_{fragment}$ is the mass of a single fragment, defined as $\rho v_{fragment}$.

In order to solve this system of equations, the value of the constant α must be determined. In a general sense, this depends on the debris behavior modeled. In this model, the debris behavior is modeled as a uniform hemispherical shell of debris pieces, expanding outward with the fragment velocity $V_{fragment}$. A cross sectional diagram of the velocity distribution is reproduced as Figure 3.3.

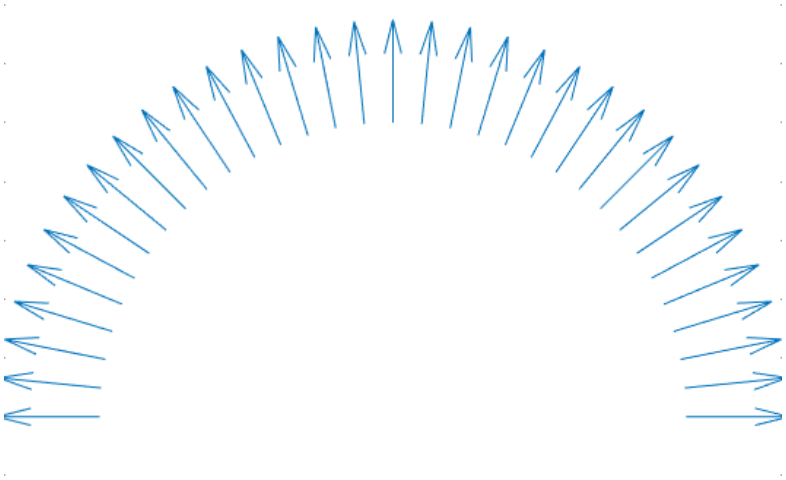

Figure 3.3. Cross Section of Uniform Velocity Distribution

To determine α in this scenario, the following surface integral must be evaluated.

$$\alpha = \frac{1}{2\pi}\int_0^{2\pi}\int_0^{\frac{\pi}{2}} \cos\varphi\,(\sin\varphi) d\varphi d\theta \tag{14}$$

In the previous equation, angles θ and φ serve to sweep out the surface of the hemispherical shell, and the cos(φ)sin(φ) term serves to isolate the vertical velocity component. Equation (14) can be simplified somewhat through trigonometric substitution into equation (15) and then solved.

$$\alpha = \frac{1}{2\pi}\int_0^{2\pi}\int_0^{\frac{\pi}{2}} \frac{1}{2}(2\sin(\varphi)\cos(\varphi)) d\varphi d\theta \tag{15}$$

$$\alpha = \frac{1}{2\pi}\int_0^{2\pi}\int_0^{\frac{\pi}{2}} \frac{1}{2}\sin(2\varphi)\, d\varphi d\theta \tag{16}$$

$$\alpha = \frac{1}{2\pi}\int_0^{2\pi} \frac{1}{2} d\theta \tag{17}$$

$$\alpha = \frac{1}{2} \tag{18}$$

Therefore, for the case for a uniform spherical shell of debris, the constant α shall be set to ½. Substituting this back into the system and rearranging both equations to be equal to zero, the final nonlinear system of equations is presented as equations (19) and (20).

$$0 = \frac{1}{2}M_{main}(\Delta V_{main})^2 + \frac{n_{fragments}}{2}m_{fragment}(V_{fragment})^2 - E_{Remainder} \quad (19)$$

$$0 = \frac{1}{2}V_{fragment}\ln\left(\frac{M_{Asteroid}}{M_{main}}\right) - \Delta V_{main} \quad (20)$$

This system of equations can then be solved by solving equation (20) for ΔV_{main} in terms of $V_{fragment}$ and then substituting into equation (19) and reducing. This yields the solutions

$$\Delta V_{main} = \frac{1}{2}V_{fragment}\ln\left(\frac{M_{Asteroid}}{M_{main}}\right) \quad (21)$$

$$V_{fragment} = \sqrt{\frac{E_{Remainder}}{\left(\frac{1}{8}M_{main}\ln\left(\frac{M_{Asteroid}}{M_{main}}\right)^2 + \frac{n_{fragments}}{2}m_{fragment}\right)}} \quad (22)$$

Equations (21) and (22) yield values for the ΔV of the main body, as well as the velocity of the fragments. These two quantities are the desired end goals of the model in most circumstances. Should the kinetic energy be desired, the velocity is easily converted using previously calculated quantities. The programs implementing this routine are available in Appendix A.

3.3. MODEL PREDICTIONS

3.3.1. Description of Test Case. As a baseline for analyzing the predictions of the model, a representative test asteroid is necessary. To ensure relevance, asteroid parameters should be chosen to somewhat replicate a potentially threatening near Earth body. This narrows down the population of possible bodies to be simulated.

Of the threatening near Earth objects, there are a number of characteristics that are shared. Of the bodies that remain to be discovered, the vast majority are smaller than 500 meters in diameter [14]. As approximately 70% of near Earth asteroids are believed to be chondritic, an asteroid on an impact course with Earth would likely have a density around 3 grams per cubic centimeter [15,16]. Finally, while the fracture energy of chondritic materials is not well-measured, it is not unreasonable to assume values in keeping with terrestrial rocks similarly composed of pyroxene and olivine. Due to the availability of data and similarities in density, the fracture energy of basalt is substituted. Combining all these parameters together, the parameters of the test case asteroid are summarized in Table 3.1 below.

Table 3.1: Model Asteroid Parameters

Asteroid Radius ($r_{asteroid}$)	100 m
Asteroid Density (ρ)	2900 kg/m^3
Fracture Energy (γ_{WoF})	0.131767 kJ/m^2

3.3.2. Model Predicted ΔV. With the test case asteroid established, the first exercise is to examine what the predicted change in the main asteroid body's velocity is post-fragmentation. This can be done quite easily by running the model over a selection of possible initial conditions of depth of fracture, and of explosive energy, as these are two of the parameters that can be most controlled. The depth of fracture is controlled by the emplacement depth of the explosives, while the explosive energy could be determined by amount and composition in cases involving conventional explosives, or through a variable yield nuclear explosive.

For the purposes of this exercise, the size of the fragments produced is held constant at a 10 cm diameter. This size is not unreasonable in controlled fragmentation events on Earth, while striking a middle ground between the possible extremes of pulverizing the fragmented section to dust, or barely fracturing the material into large boulders. While fragmentation size can be correlated to the energy applied to the

fractured volume, assuming a fixed debris size eased the construction of the model significantly.

Bringing all these considerations together, the model was run on a 100 x 100 grid of initial conditions, with explosive yield varying between zero and 5 tons TNT equivalent energy, and with the depth of the fragmented spherical cap ranging from surface depth, to the fracturing of one entire hemisphere of the asteroid. The resulting contour chart is shown Figure 3.4.

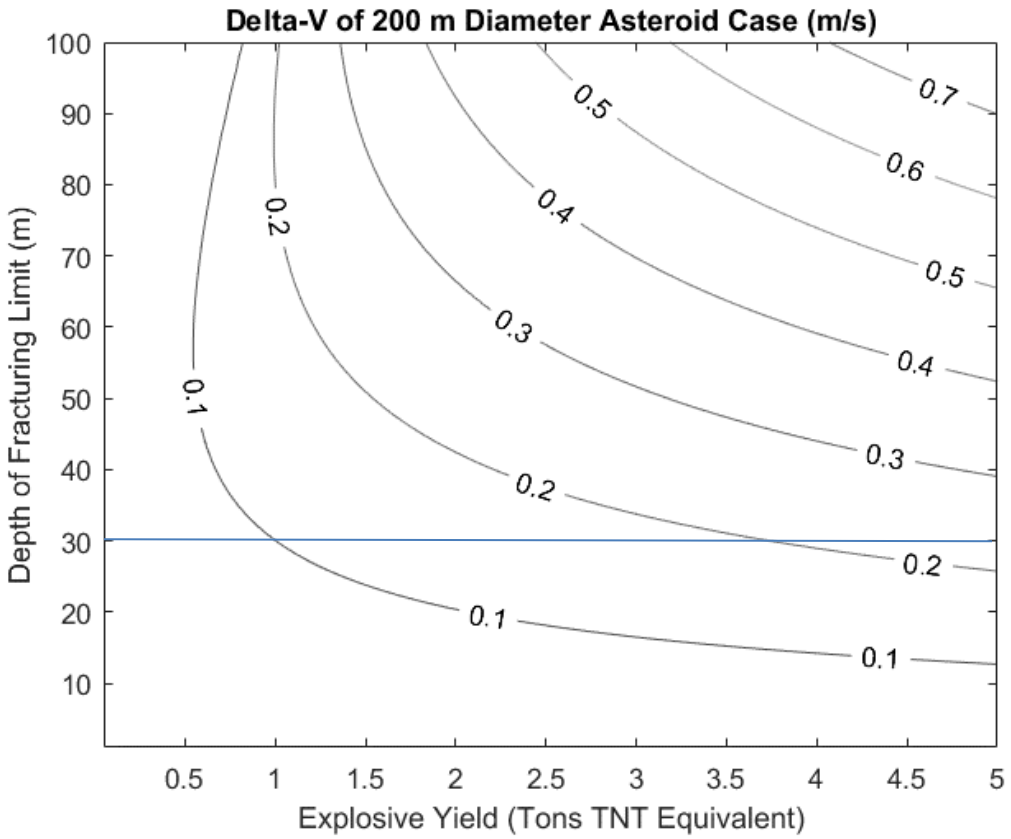

Figure 3.4. Modeled Asteroid ΔV Values

The possible deflection velocities range between 0 and just below 0.8 meters per second. However, the higher velocities are only available for fracturing depths that lead to a fracturing of a larger proportion of the asteroid body than desired. Fracturing too much of the asteroid body could lead to a shotgun-like effect, imparting insufficient velocity to disperse the fragments, peppering the Earth with debris and causing greater

damage. With restriction of the fracture depth to 30 meters, equivalent to the fracturing of six percent of the overall asteroid body volume or less, the maximum change in velocity possible is reduced to 0.23 meters per second at an energy of 5 tons TNT equivalent explosive yield. This number can be taken as a far more reasonable estimate for the modeled velocity.

3.3.3. Estimate and Modeling of Deflection Distance. In order to determine how far ahead of time the deflection velocity must be produced in order to prevent a collision, two different approaches can be considered. The first method relies on a heuristic method to estimate the deflection induced by a given perturbation. The second method available is treating the system as two separate two-body problems, and determining the minimum distance between bodies after the deflection is applied using the analytic solution for Keplerian motion.

The first approach relies on an understanding of differential changes in an orbit after a velocity increment is applied. As suggested by Ahrens and Harris, it can be calculated that the difference in position induced by an impulse along the orbital motion of the body can be estimated through

$$\delta \approx 3\Delta v t \tag{23}$$

Substituting the maximum velocity change determined previously of 0.23 meters per second, and accounting for units, this heuristic predicts a deflection of over 21,000 kilometers after just one year in time. This is the difference between a direct impact, and a three-Earth radius flyby, a significant result. Even with deflection velocities as low as 0.01 meters per second, an asteroid can be induced to miss the Earth after a decade.

To accomplish a more accurate prediction of the miss distance, it is necessary to turn to computational modeling of orbital dynamics. By modeling the system as two simultaneous two-body problems (Sun-Earth and Sun-Asteroid), the direct miss distance can be determined to a higher degree of precision. In order to do this, test asteroid orbital characteristics are needed. As an example, an asteroid whose aphelion is 1 AU and perihelion 0.75 AU was chosen. These parameters are similar to the well-known body

99942 Apophis, an Aten family asteroid whose orbit regularly brings it into Earth's vicinity including a series of close passes between 2000 and 2050.

From these orbital characteristics, the initial conditions for the model are constructed. The initial phase of modeling begins with both bodies at the collision point, represented by the initial conditions in Table 3.2. It should be noted that the initial conditions are selected so as to constrain the motion primarily to the ecliptic plane for the basic case. This fundamentally simulates a worst-case asteroid orbit, as when the two orbits are coplanar, they are far more likely to encounter a close approach.

Table 3.2. Initial Conditions for Backwards Solution

Earth x	1 AU	Asteroid x	1 AU
Earth y	0	Asteroid y	0
Earth z	0	Asteroid z	0
Earth v_x	0	Asteroid v_x	0
Earth v_y	-29.78 km/s	Asteroid v_y	-27.57 km/s
Earth v_z	0	Asteroid v_z	0

These initial conditions are then transformed into the six classical orbital elements for each body: semimajor axis a, orbital eccentricity e, orbital inclination i, right ascension of the ascending node Ω, argument of the periapsis ω, and the mean anomaly M. This system fully describes the orbits of both bodies, and also is easily propagated for a time t by incrementing mean anomaly M by an amount $n*t$, where n is the orbital mean motion. This is used to propagate the system back to the point in time at which the deflection velocity is to be applied. As the two-body problem is reversible, this effectively runs the system backwards in time, to find the initial conditions for the deflected case.

To apply the deflection velocity change to the asteroid, the orbital elements must be converted back to Cartesian coordinates. The velocity vector of the asteroid at the instant the asteroid is to be deflected by the explosive blast can then be extracted, and turned into a unit vector. Multiplying this unit vector by the desired velocity change results in a vector with magnitude equal to the desired deflection velocity, and aligned antiparallel to the asteroid's instantaneous orbital velocity in the time-forward case. Thus,

the deflection will serve to lower the asteroid's aphelion. The thrust direction is chosen as such since the asteroid's orbit is wholly contained within the orbit of Earth. Therefore, lowering the aphelion would ideally prevent any future collisions as well as the immediate collision threat.

For forward propagation of the problem with the deflection added, the end state of the previous orbit must be modified. To transform the problem back into the case where it runs forward in time, the velocity values need simply be negated. Finally, the deflection vector is added to the velocity components of the asteroid, as shown in Table 3.3.

Table 3.3. Initial Conditions for Forward Solution

Earth x	$EarthX_{end}$	Asteroid x	$AstX_{end}$
Earth y	$EarthY_{end}$	Asteroid y	$AstY_{end}$
Earth z	$EarthZ_{end}$	Asteroid z	$AstZ_{end}$
Earth v_x	$-EarthVx_{end}$	Asteroid v_x	$-AstVx_{end}+\Delta V_x$
Earth v_y	$-EarthVy_{end}$	Asteroid v_y	$-AstVy_{end}+\Delta V_y$
Earth v_z	$-EarthVz_{end}$	Asteroid v_z	$-AstVz_{end}+\Delta V_z$

These new initial conditions are then converted back to the standard orbital elements and can be propagated forward in time. At each point in time, the distance between the two bodies can be calculated, and the minimum value of the distance corresponds to the miss distance for that scenario. The orbital paths that result can be plotted to ensure that the system simulated the orbits correctly. The results of one such iteration of this process can be seen in Figure 3.5.

At the scale that the orbits in Figure 3.5 have been plotted, both the deflected and undeflected asteroid orbits overlap. The process of numerically simulating orbits and deflections, and then determining the point of closest approach is repeated, each time simulating a deflection placed at the perihelion of the asteroid orbit, one period prior to the previous simulated lead time. The results of this process are summarized in Table 3.4.

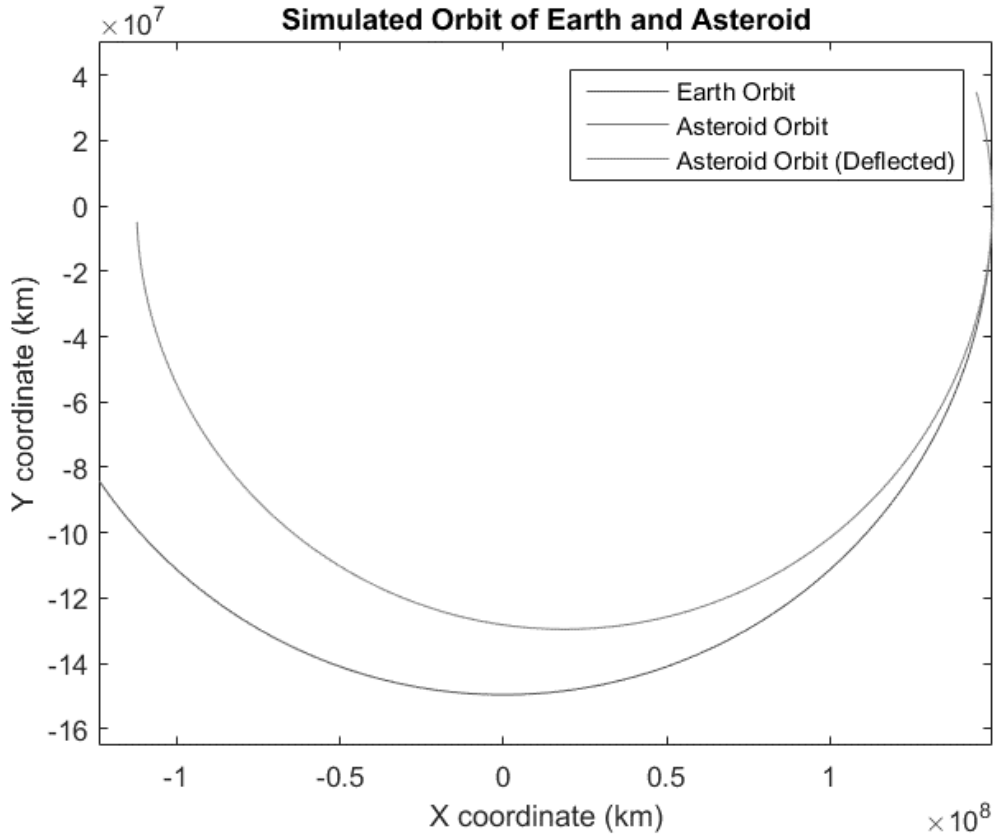

Figure 3.5. Representative Orbital Plot

Table 3.4. Example Case Deflection Distances for Perihelion Deflections

Periods	Years	Deflection Distance (km)
0.5	0.41	5774
1.5	1.22	6341
2.5	2.04	7455
3.5	2.86	10,685
4.5	3.68	62,785

Compared to the miss distance predicted by the heuristic at the beginning of this section, the improved fidelity two-body problem model is more conservative in its predictions. The deflection distance becomes greater than one Earth radius after 2.5 asteroid orbits. After this point, the distance begins to increase rapidly. After 4.5 asteroid orbits, the asteroid misses Earth by over 60,000 kilometers. This demonstrates the

importance of time in multiplying a small initial deflection in velocity into a large resultant difference in position later on.

3.3.4. Sensitivity Study. In order to better understand and quantify the effects of changing inputs on the output of a given model around a test case, a basic sensitivity study needs to be undertaken. A sensitivity study consisting of the partial derivatives with respect to model inputs shows how deviations from that test case affect the output of the model. This is especially useful when seeking to choose variables for analysis in a Monte Carlo uncertainty quantification method. Because the asteroid fragmentation model was untested at the time of initial analysis, an understanding of the input-output relationships and relative sensitivities was necessary for future test design.

As the asteroid fragmentation model requires six inputs, six first order partial derivatives are necessary to complete the sensitivity vector. So as to improve the accuracy of the solution, the 4th order center difference approach in equation (24) is used, accurate to O(h^4).

$$F'(x) = \frac{-u_{i+2}+8u_{i+1}-8u_{i-1}+u_{i-2}}{12h} \tag{24}$$

The step size for these calculations was chosen to be 10^{-4}. The resulting sensitivity vector is shown in Table 3.5.

Table 3.5. Model Sensitivities

Change w.r.t. radius	dF/dr	-0.00401
Change w.r.t. fracture depth	dF/dd	0.004335
Change w.r.t. fragment radius	dF/dr_f	0.131767
Change w.r.t. explosive yield	dF/dY	0.036109
Change w.r.t. work of fracture	dF/de	-6.59E-05
Change w.r.t. density	dF/dρ	-2.66E-05

The fragment radius r_f clearly has the strongest effect on the model's output ΔV, with the explosive yield of the fragmenting charge holding the next most sway. The asteroid radius and fracture placement depth hold a lesser but equal sway. Finally, fracture energy and material density do affect the model, but to a far lesser degree than all

the other inputs. While easily generated, this information is extremely valuable, aiding particularly in determining which parameters to vary when determining model stability.

3.3.5. Monte Carlo Uncertainty Modeling. As a number of assertions were made in the development of the asteroid fracturing model that may not necessarily prove applicable, it makes sense to do consider parametric variations so as to better understand the effects of uncertainty on the model's predictions. Therefore, a Monte Carlo process was used to assess the output response to input uncertainties.

In order to develop a Monte Carlo simulation, the input variables are isolated and modeled as distributed random variables. The earlier sensitivity analysis is invaluable in determining which inputs to model variation in. As the model was relatively insensitive to material fracture energy and material density, these parameters are fixed at their test case values, along with the radius of the asteroid itself. The other three variables are distributed normally with their distribution parameters characterized in Table 3.6.

Table 3.6. Variable Distributions for Monte Carlo Process

	Mean	σ
Fracture Depth	30 (m)	2 (m)
Fragment Radius	0.1 (m)	0.02 (m)
Explosive Yield	2.5 (t TNT)	0.125 (t TNT)

With the input variable distributions modeled, the only matter remaining is to run the model a sufficient number of times to develop the statistical distribution. For the purposes of this test, $n = 10^5$ is chosen, to balance statistical significance with computational run time. The generated output distribution histogram is presented in Figure 3.6, along with Table 3.7 showing statistical measures calculated from the histogram distribution.

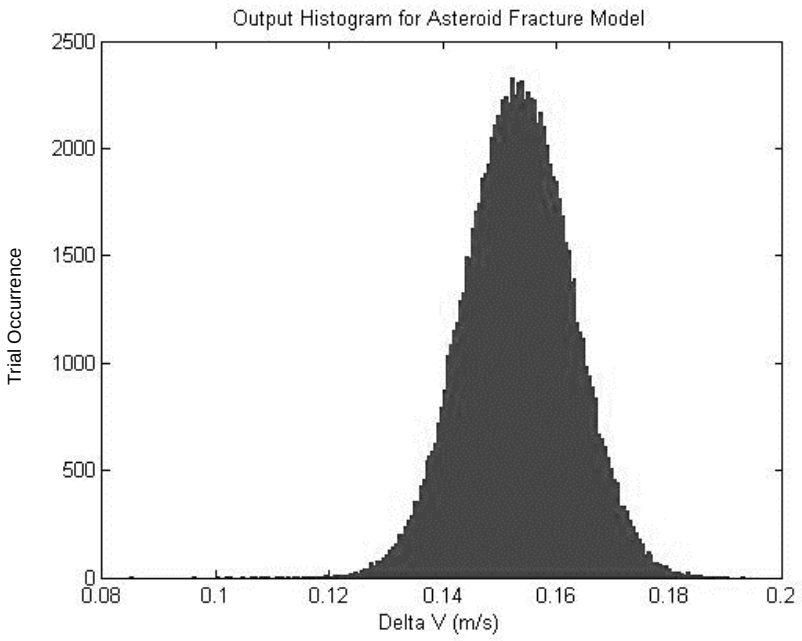

Figure 3.6. Histogram of Output Statistical Distribution

Table 3.7. Output Statistical Measures

Mean	0.153373	
σ	0.009401	
2σ Interval (95%)	0.134571	0.172174
Skewness	-0.04417	

As can be seen in the histogram, the output distribution is essentially normally distributed, most likely due to the dominating effect of fragment radius on the model. The statistical mean correlates closely to the case result for the equivalent deterministic test case, and the 95% confidence interval brackets the mean reasonably closely. For the future development of physical test cases, these results bode well for the possibility of predictable modeling.

3.3.6. Effects of Uncertainty in Thrust Direction. Due to factors such as a fast rotating asteroid body, or an asymmetrical fragmentation event, it is possible that the intended deflection velocity could be applied in a direction differing from the generally preferable parallel orientation. Due to the sensitive nature of orbital dynamics, the deflection distance of such a case would be expected to change. As any change in

deflection distance could be a matter of significant destruction, it is best that these effects be quantified beforehand.

In order to quantify the effects of such a difference in direction, an analysis similar to the one in Section 3.3.3 is undertaken. Instead of applying the velocity change directly antiparallel to the instantaneous velocity of the asteroid at the deflection point, the deflection is applied rotated ten degrees relative to the initial deflection direction. For simplicity, the rotations are chosen to take place around the Cartesian x and z axes. The effects of these rotations on a 2.5 period deflection case are collected in Table 3.8.

Table 3.8. Effects of Angular Deviation on Deflection Distance

Deflection Offset (Right Hand Rule)	New Deflection Distance (km)
Baseline	7455
10° X axis+	7392
10° X axis-	7392
10° Z axis+	7409
10° Z axis-	7375

The effects of a ten degree rotation on the deflection distance in the 2.5 period case are fairly minimal. The worst-case scenario is the rotation around the Z axis in the negative sense, and even at worst results in only a one percent change in deflection distance. This shows that the deflection of the asteroid is not overly sensitive to small inaccuracies in the deflection velocity direction, which is promising considering the possible uncertainties in deflecting an asteroid.

4. DEVELOPMENT OF TESTABLE MODEL

4.1. CONSTRAINTS ON TESTABILITY

In order to transition from an abstract model to the realm of testability, the constraints necessary to enable testing must be well understood. Prime amongst these considerations is constructability. Any system that is difficult to construct, or that requires materials which are not easily available, is impractical to pursue.

In an ideal world the material properties of any simulant chosen for fracture testing will approximate those of an actual asteroid. Unfortunately, the material properties of the vast majority of smaller asteroids are not well characterized if at all. Least well known amongst those qualities is the bulk fracture energy. While it has already been shown that the model is not overly sensitive to changes in fracture energy, it would still be preferable to have a simulant material that displays characteristics that could not be unreasonable for asteroid material to possess.

Finally, the explosive impulse modeled must be equivalent to one produced by available hardware. This helps with comparison between model and physical domains. However, as explosive energies are well understood, it is primarily important that the amount of explosives used only fracture a portion of the test body, rather than obliterating it completely or not fracturing it at all. As this is best determined through physical testing, a preliminary round of blast chamber testing was necessary to optimize explosive yield.

4.2. CONSTRUCTING A TESTABLE SYSTEM

4.2.1. Casting and Construction of Test Blocks. Keeping in mind the constraints, a block size of 8 inches (20.32 cm) on a side was selected for testing. This size combines ease of measurement and manufacture with moderate weight for transportability, but is large enough to not be entirely obliterated by small amounts of explosives.

As data on small asteroid material properties are not well known, the choice was made to select a block material that has properties reasonably similar to rock but that is easily castable and readily available. To that end, cement was chosen as a simulant material. With a nominal density of 1.5 kg/L, and a work of fracture of 115 J/m^2 (compare to 3 kg/L and ~130 J/m^2 for a stony meteorite), cement is approximately half as dense than most stony meteorites, but displays fracture characteristics that could reasonably be expected from a stony material.

Blocks were cast in sets of five, using plywood molds to ensure regularity. Cement was mixed according to standard practice, with a ratio of 0.5 kg water to every kg of cement mix. Molds were greased prior to cement addition to ease later removal, and filled level. After curing in the mold for a week, blocks were removed and set aside to cure further. A total of 35 blocks were produced.

4.2.2. Static Fracture Testing. Two separate varieties of blasting caps were made available for testing. Both the Electric Super caps (labeled henceforth as Type A) and the DigiShot caps (Type B) contained the same weight of PETN explosive, but had differences in case construction and dimension. In order to determine the fracturing capacity of the two types of available blasting caps, a short series of blast chamber tests was run. Four selected blocks each had a single quarter-inch diameter borehole drilled into them, two with a depth of one inch, and two with a depth of three inches. As there were two available detonation options, each detonator type was detonated at both depths. The blocks were individually placed into the blasting chamber, with the loaded borehole facing upwards. After sealing of the chamber door, the explosive was detonated, and after the chamber air was exhausted, the block and any fragments were retrieved.

Analysis of the post detonation blocks was quite informative. The shallow bore blocks in both cases show minimal cracking of the block body as a whole, with small conical craters to varying depths. In the deep bore case, the explosives within the detonators proved sufficient to fragment the upper half of the block. These results can be seen in Figure 4.1. The two blocks of the upper left of the image were tests of detonator A, while the lower right blocks were tests of detonator B.

Figure 4.1. Static Fragmentation Test Blocks From Preliminary Testing

The A detonators proved to be significantly less powerful in both tests. The shallow bore test case barely produced any ejecta, while the deep bore case only split the block into several large blocks, without displacing much ejecta. This behavior is likely due to the fact that the A type detonators had an outer diameter that was slightly smaller than the bore diameter, leading to a weaker energy transfer between explosive and block. As the criterion for success was adequate production of ejecta, the A detonators were removed from consideration.

The B type detonators produced ejecta at both depths far more reliably. The shallow bore test excavated and ejected debris from a roughly conical crater of equal depth to the borehole. The deeper case extensively fractured the whole block mass, while again ejecting small debris from a conical crater down to the borehole depth. This crater

is clearly evident in Figure 4.1, where the reconstructed block is at the bottom of the image. While the explosive charge fractured more of the block than would be ideal, the charge did a much better job of ejecting debris. For this reason, the type B detonators were selected for use in further testing.

4.3. MODEL CONSTRUCTION

The testable model is functionally identical to the model outlined in Section 3.2, with the following changes. Firstly, the body geometry of the original body must be modified to model a cube of side length *s*, rather than a sphere. Therefore equation (1) is rewritten as

$$V_{Block} = (s)^3 \tag{25}$$

The mass of the block is calculated from density as in the original model, but an additional constant to account for the mass of testing apparatus appears in the testable variant.

$$M_{Whole} = \rho_{Block} V_{Block} + M_{apparatus} \tag{26}$$

The geometry of the region fractured by explosives is also changed to better match the results of testing. In the tests, the debris was mainly excavated from a conical crater as deep as the borehole, and with a base radius of twice its depth. Therefore, the fractured volume is now given as

$$V_{Fractured} = \frac{4\pi}{3}\, d^3 \tag{27}$$

The remainder of the model proceeds identically to the one described in Section 3.

4.4. MODEL PREDICTIONS

The model was run under conditions designed to replicate the conditions of testing. Explosive energy was set to replicate the explosive content of the chosen detonators, while the material parameters were set to replicate the cast blocks. The set of initial conditions for the model is contained in Table 4.1.

Table 4.1. Testable Model Initial Conditions

Side length	s	0.2032 m
Fragment Radius	r_f	0.0001 m
Explosive Energy	Y	5112 J
Work of Fracture	γ_{WoF}	110 J/m^2
Density	ρ	1800 kg/m^3

In order to have a range of different conditions to test against, the model checks four different borehole depths, in half inch increments from zero inches to three inches in depth. The Matlab routines used to run the model are available in Appendix B. The model's predictions for the final velocity for the main body are plotted in Figure 4.2.

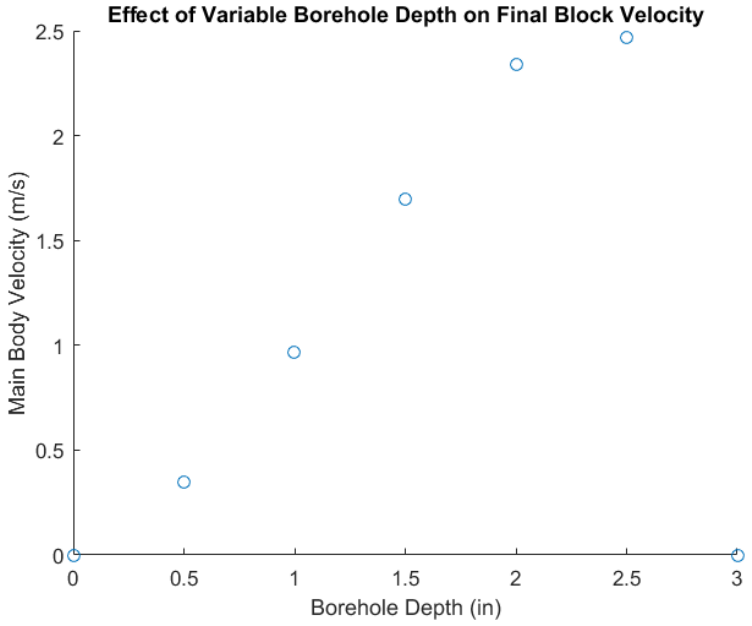

Figure 4.2. Effect of Variable Borehole Depth on Final Block Velocity

The model predicts a smoothly increasing velocity trend, reaching a point of maximal velocity of ~2.5 m/s at 2.5 inches borehole depth. Beyond this depth, the explosive energy becomes insufficient to fracture the modeled volume, and the model predicts zero change in block velocity. This matches with intuition, as a small enough explosive will only crack the material without displacing it.

The modeled block velocities appear higher than could be reasonable, given the small amount of explosive used in the modeled blast. This possible error could be due to multiple sources. Prime among the possible sources is that the debris in the model has been treated as smooth spheres, which is a case that minimizes fracture surface area. Natural fracture geometries would generate significantly more area per volume. Also likely is that in a real world case, energy transfer between the explosive and the block would be less than 100 percent efficient. However, neither of these quantities is easily predicted, and therefore physical testing is necessary.

5. TESTING PROCEDURE AND RESULTS

5.1. TESTING DESIGN

In order to test the predictions of the numerical model as developed, a physical experiment was necessary. Comparisons between the velocities predicted in computational modeling and the velocity resulting from a real-world detonation can provide insight into the viability of the model, as well as predicting further avenues for model improvement.

A number of options were considered for possible test designs. Static block tests would allow for analysis of the block fragmentation characteristics and ejecta analysis, but would be unable to capture the whole body motion of the block following detonation. It would also be extremely difficult to capture the energy transfer to the block, even with complicated load cell setups. A second option considered was some variation of a block-on-cart setup. This would allow for a better capturing of the dynamic block response while not constraining blast ejecta. However, the experimental setup for cart testing would be prohibitively complicated, and a significant number of unknowns could affect the testing outcome.

After much consideration, a ballistic pendulum was chosen to test energy transfer. A ballistic pendulum is an assemblage that suspends a test article in a configuration such that it can swing freely in one direction while constraining motion in all other directions. While this may constrain the ejecta behavior in undesirable ways, the dynamics governing pendulum behavior are simple and very well understood. This allows for easy analysis of energy transfer in practical implementations by measuring the maximum angle achieved during the pendulum swing. To cradle the block, a sheet steel box is affixed at the end of the pendulum arm, visible in Figure 5.1.

To measure the maximum angle of the swinging pendulum arm and thereby the energy transferred from the explosive to the main block, two independent methods of measurement were used. Firstly, a simple friction needle indicator was affixed above the pendulum. This indicator is pushed along by the swinging pendulum arm until the point of maximum angle, but remains in place due to friction with the backing plate when the

pendulum arm reverses direction. The indicator markings allow for measurement of the maximum swing angle to the nearest quarter-degree. Secondarily, a grid with two inch markings was placed standing behind the pendulum. Through analysis of high speed camera footage of each test, it is possible to measure the maximum swing angle of the pendulum from the known arm length measurements and the distance displaced on the grid.

The test apparatus was constructed out of steel, for ease of welding. The completed apparatus can be seen in Figure 5.1, taken on site the day of the testing. The angle indicator and the visual grid behind the pendulum arm are both clearly visible. The frame was not anchored to the ground as the mass of the frame was sufficient to prevent undesired motion during testing.

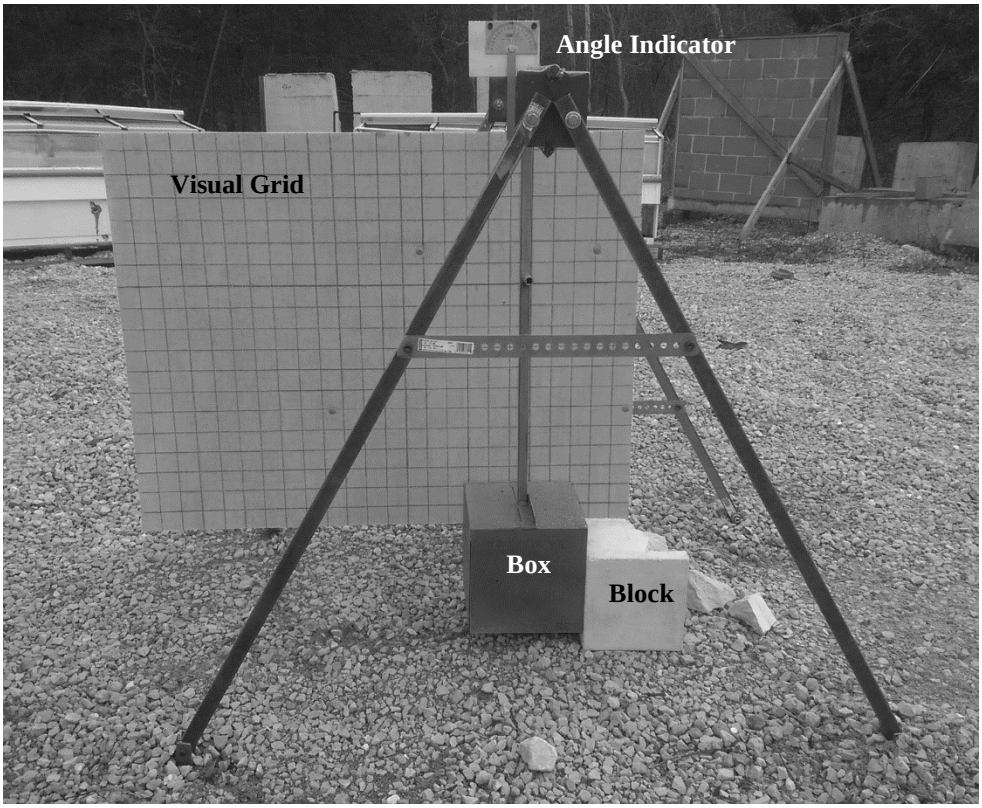

Figure 5.1. Ballistic Pendulum Test Apparatus

5.2. TESTING PROCEDURE

5.2.1. Field Testing Procedure. All field testing took place at the quarry portion of the Missouri University of Science and Technology Experimental Mine. The testing process starts with the loading of a block with a predrilled borehole into the box at the base of the pendulum. The borehole opening is horizontal, and is positioned facing outward on the open side of the box. The detonator is then inserted snugly into the borehole. In the zero depth case, a small collar of putty is used to affix the detonator to the face of the block instead. After ensuring that the pendulum arm has settled into a motionless vertical position, the maximum angle indicator is reset to zero. All exterior personnel must retreat to a blast safe structure before the detonator can be connected to the control box. The high speed camera is then readied. At this point, the experiment is primed.

After the surrounding area is alerted to the impending detonation, the high speed camera is triggered, and the detonator is set off immediately afterward. The high speed camera captures two seconds of footage and stops automatically. The footage is then saved. Once the test site is clear of dust, it is possible to return to the pendulum. The maximum angle indicator is read and recorded, and the remnant of the block and any fragments are cleared out of the block box. The process is then repeated for all blocks.

5.2.2. Procedure for Analysis. In order to be useful for comparing to the results produced by the model, the raw data from explosive testing need to be processed. The model produces results in terms of velocity, while the maximum angle of the pendulum's swing θ was measured during physical testing. Fortuitously, there is a simple means of calculating the maximum velocity of a pendulum from the maximum height of its swing. Firstly, the energy of the pendulum is calculated with

$$E_{Pendulum} = mgy(1 - \cos(\theta)) \tag{28}$$

where *y* is the center of mass of the combined pendulum and block assembly and *m* is its mass. The calculation of these quantities is found in Appendix C. Then the velocity at the base of the swing is calculated using

$$V_{Pendulum} = \sqrt{\frac{2E_{Pendulum}}{m}} \tag{29}$$

This completes the analysis necessary for calculating the pendulum velocity from the direct angle measurement. However, some additional analysis is necessary to convert the high speed footage into an angle measurement.

To produce a maximum swing angle from analysis of the high speed camera footage, two still shots are necessary. The first still is taken from the pre-detonation state of the system, and is used to find a baseline point for comparison. A representative pre-detonation still image is shown in Figure 5.2.

The second still is taken from a point determined by visual inspection of the footage as being closest to the point of maximum swing. As the pendulum slows as it reverses directions near the maximum angle, the exact frame chosen is not essential. A representative still from maximum swing can be found on the following page as Figure 5.3.

From these two images, the difference in horizontal position Δx is determined by counting the horizontal lines between the positions of the center of the block box in the two frames. This position is estimated by visual inspection to within one quarter of the grid width. The measurement in units of grid width can be multiplied by the grid measure m_{grid} to produce a dimensioned horizontal displacement, and the angular displacement is found together using

$$\theta = \sin^{-1}\left(\frac{\Delta x * m_{grid}}{y}\right) \tag{30}$$

This angle can then be applied to equations (28) and (29) to produce a velocity measure.

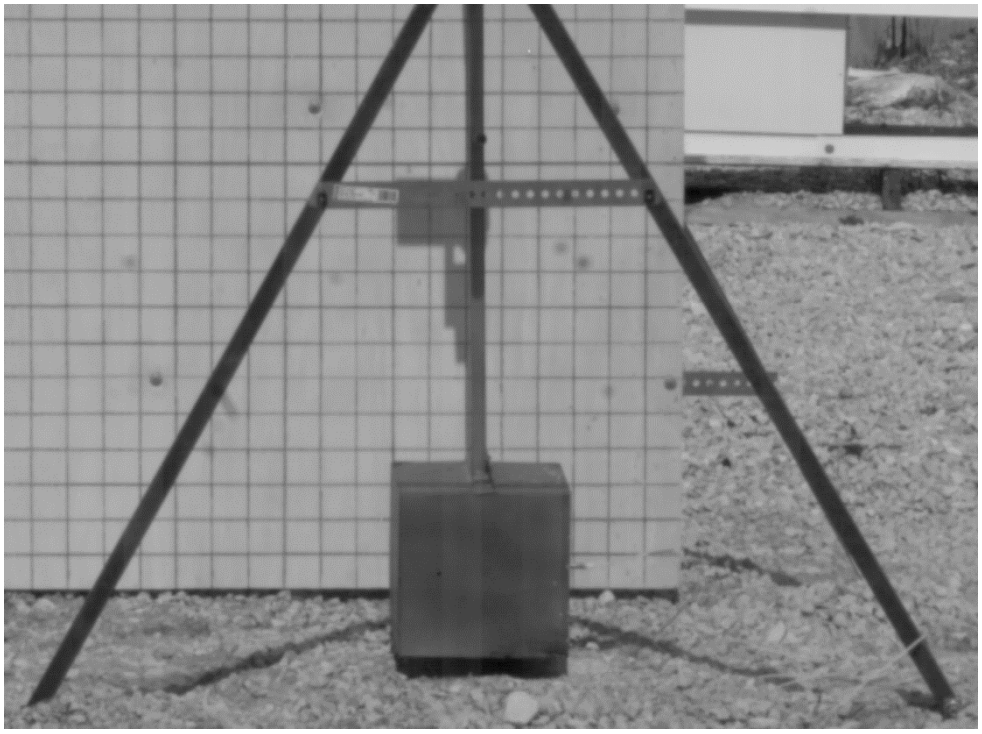

Figure 5.2. At Rest Pendulum Position

Figure 5.3. Swing Halt Position ($\Delta x = 2$)

5.3. COMPARISON TO MODEL RESULTS

The experimental results can now begin to be compared against those predicted by the model in Section 4. The average velocities measured using the angle indicator, as well as calculated by photoanalysis, are tabulated in Table 5.1. The full listing of experimental results can be found in Appendix D. The plotted comparison between the values produced by the two methods along with 2σ error bars is presented as Figure 5.4.

Table 5.1. ΔV Measured With Two Methods

Bore Depth (in)	Indicated ΔV (m/s)	Photoanalysis ΔV (m/s)
0	0.12	0.14
0.5	0.16	0.20
1	0.18	0.23
1.5	0.25	0.31
2	0.31	0.40

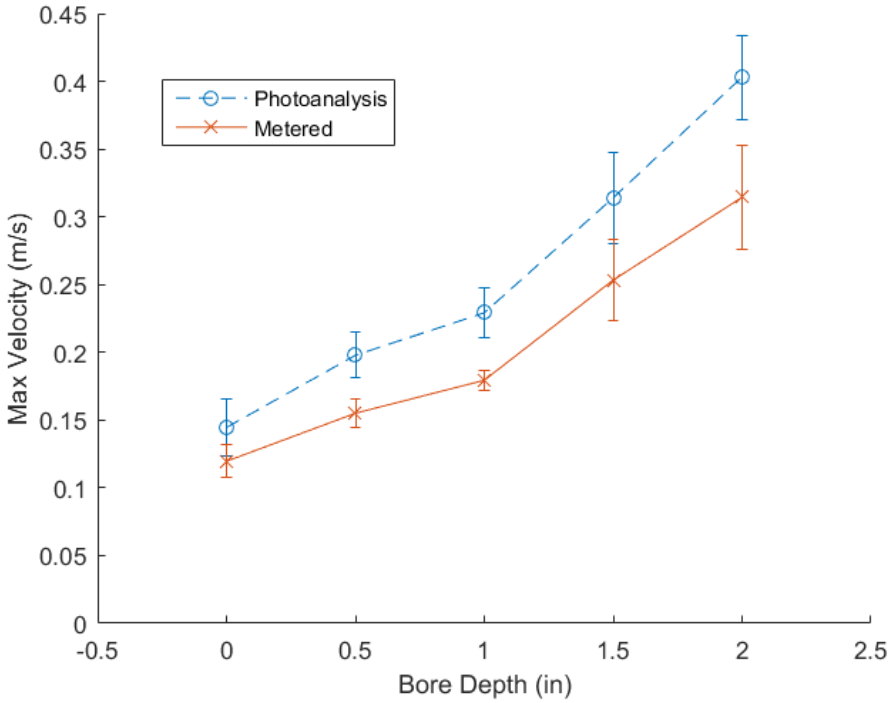

Figure 5.4. Comparison Between ΔV Measurements

As can be seen in the comparison plot, the two methods broadly agreed on the deflection velocity produced in explosive testing. However, in all cases, the photoanalytic velocity was calculated as being slightly higher than the velocity derived from direct angle measurements. This can be attributed in some degree to flexing of the pendulum arm under the impulse loading of detonation. This effect presents itself particularly in the two inch deep borehole tests, where visible flexing and oscillations of the pendulum arm are plainly visible in high speed camera footage. For the purposes of further comparison, the higher velocity is assumed to be the better of the two estimates, as it approximately compensates for the flexure of the pendulum arm.

When the comparison between the model and testing data is viewed, the results do not bode well for the model in its current incarnation. Looking at Figure 5.5, the striking difference between prediction and test data becomes clear. The model underpredicts the change in velocity for a surface detonation, and greatly overpredicts the velocity produced by deeper borehole tests. However, with some further analysis, it is possible to glean some data from the results that might show the way towards a better model.

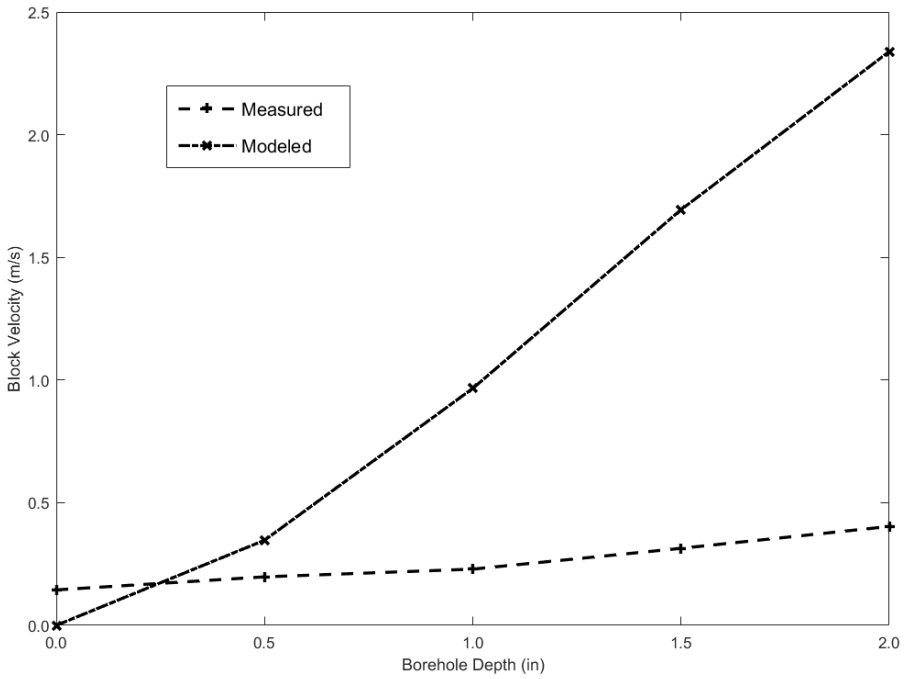

Figure 5.5. Comparison of Modeled and Measured Velocities

A basic correction of the modeled data can be done so as to quantify the differences between model and test. In this case, the correction is assumed to take the form

$$Model_{Corr}(d) = a + b * Model(d) \tag{31}$$

This rough correction allows for two parameters *a* and *b*, which correct for errors in the zero offset and rate of change in the velocity produced, respectively. If some combination of parameters can be found that leads to a better match between model and test data, then the parameters can offer some insight as to how to correct the model for future research.

The parameters *a* and *b* were selected by setting *a* so that the modeled first value agreed with measured result, and then *b* was determined through least squares minimization. The selection of 0.15 for *a* and 0.1 for *b* leads to the corrected system plotted in Figure 5.6. This newly corrected system tracks the physical test data to a much higher degree, and therefore would better seem to explain the system. With this shown, the meanings of the corrective factors can be analyzed.

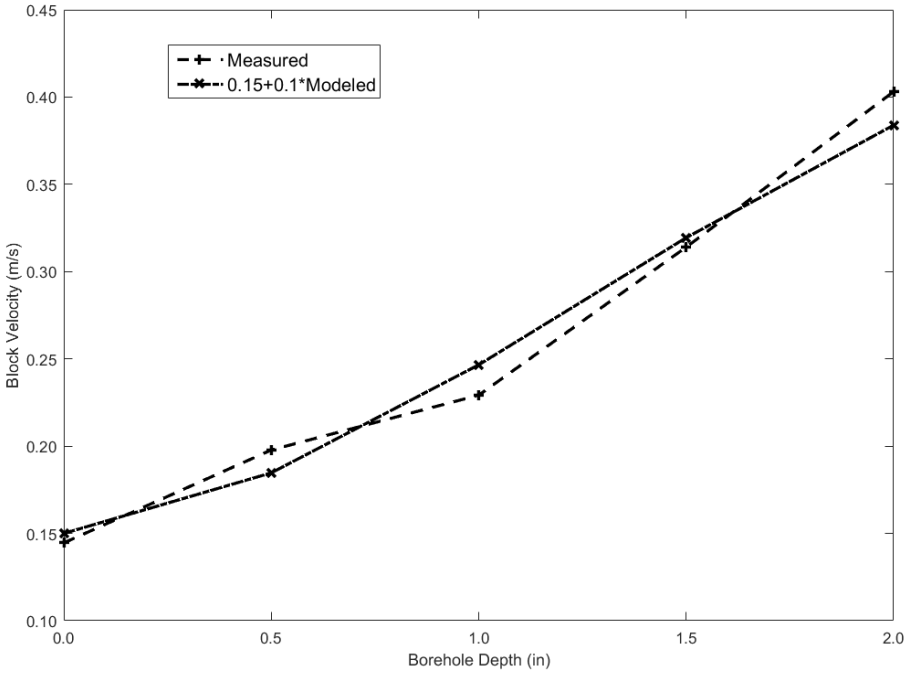

Figure 5.6. Corrected Model

The value of *a*, which corrects for the zero depth error, most likely comes from the assumptions made about the behavior of explosives in the earlier development of the model. Explosives for the purposes of the model are treated simply as sources of energy, while their real world behavior is more complex. Explosives both release shock energy directly into the rock around them, as well as producing hot gases which expand, pushing any material around them away. In neglecting the gas expansion, the original model neglected one of the sources of energy, which can induce some velocity even when no debris is produced. A version of the model that somehow accounts for this gas expansion would likely remove the need for this correction.

The intrinsic meaning of the factor *b*, which serves to correct the model slope, is less apparent. However, in general terms, *b* can be seen as a measure of the inefficiencies in energy conversion between the explosive and the kinetic energy of the rock. This inefficiency could come from many sources, including mis-estimating of the fractured area produced or of the fractured region shape as a whole, or the neglect of some efficiency factor in conversion between chemical explosive energy and the practical energy available to fracture and move rock. Better understanding of the explosive and fracture dynamics at play could therefore help roll this factor into the model itself.

The model as written clearly shows promise, but the existing errors must be resolved if the model is to be of practical use in modeling the deflection of asteroids by engineered explosive fragmentation.

6. CONCLUSIONS

6.1. WORK ACCOMPLISHED

The end goal of this thesis study has been the development and testing of a fracture energy-based model of asteroid deflection through explosive blasting for use in the study of planetary defense. To facilitate this, an overview of the state of current research was presented.

A basic model of the behavior of an asteroid under explosive impulse was then derived. The developed model calculates the energy necessary to fracture a defined volume of the asteroid, and then proportionately distributes the remaining energy. This model was then successfully applied to a simulation of deflecting an impacting body. However, some of the geometric assumptions behind the model rendered it difficult to test as constructed.

The geometric assumptions behind the model were then altered so as to increase the ease of testing. Additionally, small scale explosive tests were undertaken to refine the geometry of the region fractured by explosive blasting as well as select an explosive for use in further testing. The modified model was then used to predict the velocity change produced in a test block after explosive detonation.

Physical testing of the system previously simulated was then carried out, using a ballistic pendulum to assess the energy transfer from the explosive to the unfractured portion of the test block. Two independent methods of measuring the pendulum swing angle were employed to aid in assessing the maximum swing of the assemblage. Both measurements of the maximum swing angle were then used to calculate the energy of the swinging pendulum, and the initial velocity imparted upon the pendulum by the explosives.

A comparison between the physical testing and model predictions showed that the predicted block/asteroid velocities were much higher than those shown through physical testing. This error behavior is undesirable, as it leads to predictions of a safe deflection in cases where impact would not be avoided. The error is most likely attributable to the assumptions made about the new surface area produced by explosive rock fragmentation,

the forces produced by expanding gas, and the efficiency of energy transfer between chemical explosive energy and kinetic energy.

6.2. SUGGESTIONS FOR FUTURE WORK

The developed fracture energy model of asteroid deflection is important as it could have significant implications for the possibility of deflecting small asteroids relatively close to the projected impact date. To develop the model further and improve its accuracy, additional refining information is necessary.

Specifically, the present technique for estimating the geometry of the fragments produced in blasting could be modified to better account for the fracture geometry produced by explosive blasting. This includes the geometry of the debris particles produced, as well as the overall geometry of the fractured region as a whole.

Additionally, a better means of estimating the energy transfer between the explosives and the rock body could be implemented. This would improve upon the currently unrealistic assumptions of the model, and could also improve the modeling of the velocity distribution of the debris.

Finally, a better understanding of the material properties of stony asteroids and the development of a fracture-similar simulant would enable further testing of the model under material conditions more similar to asteroid conditions.

APPENDIX A.
ASTEROID DEFLECTION MODEL ROUTINES

asteroidsplitter.m

Implements developed model of asteroid ΔV in Matlab 2015

```
function [DeltaV,FragV] =
asteroidsplitter(r,d,rf,expyield,Efract,rho)
fragvolume = ((pi.*d.^2)./3).*(3.*r-d);
particlearea = 4*pi*(rf).^2;
particlevolume = (4/3)*pi*(rf).^3;
numparticles = fragvolume./particlevolume;
area = numparticles.*particlearea;
totalvolume = (4/3)*pi.*r.^3;
Eminimum = Efract.*area;
fragmass = rho.*fragvolume;
if (Eminimum>expyield)
    DeltaV = 0;
    FragV = 0;
else
    remainenergy = expyield-Eminimum;

    F = @(X) [0.5*(totalvolume-
fragvolume)*rho*(X(1,1)^2)+(numparticles/2)*particlevolume*
rho*(X(2,1)^2)-remainenergy;
0.5*X(2,1)*log(totalvolume./(totalvolume-fragvolume))-
X(1,1)];
    H = @(X) [(totalvolume-
fragvolume)*rho*X(1,1),numparticles*particlevolume*rho*X(2,
1);-1,0.5*log(totalvolume./(totalvolume-fragvolume))];

    X0 = [sqrt(remainenergy/((totalvolume-
fragvolume)*rho));sqrt(remainenergy/(fragvolume*rho))];

    [V,~] = NonlinearSolver(F,H,X0,15,1000);
    DeltaV = V(1,1);
    FragV = V(2,1);

end
```

TestDV.m

Plots contour chart of deflection ΔV in Matlab 2015

```
clear
close all
clc

% Chosen simulation parameters
resolution = 500;

% Chosen asteroid constants
r = 100;
Efract = 50;
rho = 2900;

% Explosive energy to split asteroid in half
expmax = 5*4.184*10^9;

yieldstep = expmax/resolution;
radiusstep = r/resolution;

for dr=1:resolution
    for de=1:resolution

dvmap(dr,de)=asteroidsplitter(r,dr*radiusstep,de*yieldstep,
Efract,rho);
    end
end
x = yieldstep/(4.184*10^9)*(1:resolution);
y = radiusstep*(1:resolution);
[c,~] =
contour(x,y,dvmap,[0.01,0.05,0.1,0.2,0.3,0.4,0.5,0.6,0.7,0.
8],'ShowText','on');
title('Delta-V of 200 m Diameter Asteroid Case (m/s)')
xlabel('Explosive Yield (Tons TNT Equivalent)')
ylabel('Depth of Fracture Plane (m)')
```

AsterSim.m

Simulates two body models of asteroid and Earth in Matlab 2015

```
clear
clc
close

format long g

% Constants

mu = 1.32712440018*10^11;
window = 24*60*60;

yearinseconds = 365.256363004*86400;
pearth = 1*yearinseconds;
rearth = ((mu*pearth^2)/(4*pi()^2))^(1/3);
vearth = sqrt(mu/rearth);
aaster = (1.75/2)*rearth;
vaster = sqrt(mu*((2/rearth)-(1/aaster)));
paster = 2*pi()*sqrt(aaster^3/mu);

earthrad = 6371;
dv = 0.3/1000;

% Initial Conditions
x1i = rearth;
y1i = 0.01;
z1i = 0.01;
u1i = 0.01;
v1i = vearth;
w1i = 0.01;
R1i = [x1i y1i z1i -u1i -v1i -w1i];

x2i = rearth;
y2i = 0.01;
z2i = 0.01;
u2i = 0.01;
v2i = vaster;
w2i = 0.01;
R2i = [x2i y2i z2i -u2i -v2i -w2i];

[OE1i(1),OE1i(2),OE1i(3),OE1i(4),OE1i(5),OE1i(6)] =
xyztoclassic(R1i(1:3),R1i(4:6));
[OE2i(1),OE2i(2),OE2i(3),OE2i(4),OE2i(5),OE2i(6)] =
xyztoclassic(R2i(1:3),R2i(4:6));
```

```
for Periods = 1:9

T = (Periods-0.5)*paster;

OE1m = [OE1i(1:5),OE1i(6)+T.*sqrt(mu./rearth^3)];
OE2m = [OE2i(1:5),OE2i(6)+T.*sqrt(mu./aaster^3)];

R1m =
classictoxyz(OE1m(1),OE1m(2),OE1m(3),OE1m(4),OE1m(5),OE1m(6
));
R2m =
classictoxyz(OE2m(1),OE2m(2),OE2m(3),OE2m(4),OE2m(5),OE2m(6
));

vec = R2m(4:6);
unitfactor = sqrt(vec(1)^2+vec(2)^2+vec(3)^2);
unitv = vec./unitfactor;
delta = dv.*(unitv);
angle = -10*pi()/180;
deltarot = ([cos(angle),-
sin(angle),0;sin(angle),cos(angle),0;0,0,1]*(delta.')).';

R1n = [R1m(1:3),-R1m(4:6)];
R2n = [R2m(1:3),-R2m(4:6)+deltarot];

[OE1n(1),OE1n(2),OE1n(3),OE1n(4),OE1n(5),OE1n(6)] =
xyztoclassic(R1n(1:3),R1n(4:6));
[OE2n(1),OE2n(2),OE2n(3),OE2n(4),OE2n(5),OE2n(6)] =
xyztoclassic(R2n(1:3),R2n(4:6));

iters = 1;

panew = 2*pi()*sqrt(OE2n(1)^3/mu);
Tnew = (Periods-0.5)*panew;

for t = Tnew-window:30:T+window
    OE1f = [OE1n(1:5),OE1n(6)+t.*sqrt(mu./rearth^3)];
    OE2f = [OE2n(1:5),OE2n(6)+t.*sqrt(mu./OE2n(1)^3)];

    R1f =
classictoxyz(OE1f(1),OE1f(2),OE1f(3),OE1f(4),OE1f(5),OE1f(6
));
    R2f =
classictoxyz(OE2f(1),OE2f(2),OE2f(3),OE2f(4),OE2f(5),OE2f(6
));
```

```
    dist(iters,1) = sqrt((R2f(1)-R1f(1))^2+(R2f(2)-
R1f(2))^2+(R2f(3)-R1f(3))^2);
    dist(iters,2) = t;

    iters = iters+1;
end

mindist = min(dist(:,1));

dists(Periods,:) = [mindist,Periods-0.5]

end
```

AsteroidSensitivity.m

Computes sensitivities vector for model in Matlab 2015

```
clear
clc
close all

F1 = @(x)
asteroidsplitter(x,30,.1,2.5*4.184*10^9,200,2900);
F2 = @(x)
asteroidsplitter(100,x,.1,2.5*4.184*10^9,200,2900);
F3 = @(x)
asteroidsplitter(100,30,x,2.5*4.184*10^9,200,2900);
F4 = @(x)
asteroidsplitter(100,30,.1,x*4.184*10^9,200,2900);
F5 = @(x)
asteroidsplitter(100,30,.1,2.5*4.184*10^9,x,2900);
F6 = @(x) asteroidsplitter(100,30,.1,2.5*4.184*10^9,200,x);

df1 = CDiff(F1,100,0.0001);
df2 = CDiff(F2,30,0.0001);
df3 = CDiff(F3,.1,0.0001);
df4 = CDiff(F4,2.5,0.0001);
df5 = CDiff(F5,200,0.0001);
df6 = CDiff(F6,2900,0.0001);

S = [df1;df2;df3;df4;df5;df6]
```

AsteroidMonte.m

Uses Monte Carlo process to generate model uncertainty histogram in Matlab 2015

```
clear
clc
close all

for n=1:100000
    r = 100;
    d = normrnd(30,2);
    rf = normrnd(.1,.02);
    expyield = normrnd(2.5*4.184*10^9,1.25*10^8);
    Efract = 50;
    rho = 2800+200*rand();
    data(n) = asteroidsplitter(r,d,rf,expyield,Efract,rho);
end

hist(data,200)
mu = mean(data);
sig = std(data);
confinterv = [mu-2*sig,mu+2*sig];
skew = skewness(data);

stat = [mu,0;sig,0;confinterv;skew,0]
```

APPENDIX B.
TEST MODELING ROUTINES

testsplitter.m

Implements model of lab test as described in Section 3 in Matlab 2015

```
function [DeltaV,FragV,Emain,Efrag] =
testsplitter(s,d,rf,expyield,Efract,rho,Mequip)
fragvolume = (4/3)*pi*d^3;
particlearea = 4*pi*(rf).^2;
particlevolume = (4/3)*pi*(rf).^3;
numparticles = fragvolume./particlevolume;
area = numparticles.*particlearea;
totalvolume = s.^3;
Eminimum = Efract.*area;
fragmass = rho.*fragvolume;
if (Eminimum>0.25*expyield)
    DeltaV = 0;
    FragV = 0;
    Emain = 0;
    Efrag = 0;
else
    remainenergy = 0.25*expyield-Eminimum;

    F = @(X) [0.5*((totalvolume-
fragvolume)*rho+Mequip)*(X(1,1)^2)+(numparticles/2)*particl
evolume*rho*(X(2,1)^2)-remainenergy;
0.5*X(2,1)*log((totalvolume*rho+Mequip)./((totalvolume-
fragvolume)*rho+Mequip))-X(1,1)];
    H = @(X) [((totalvolume-
fragvolume)*rho+Mequip)*X(1,1),numparticles*particlevolume*
rho*X(2,1);-
1,0.5*log((totalvolume*rho+Mequip)./((totalvolume-
fragvolume)*rho+Mequip))];

    X0 = [sqrt(remainenergy/((totalvolume-
fragvolume)*rho+Mequip));sqrt(remainenergy/(fragvolume*rho)
)];

    [V,~] = NonlinearSolver(F,H,X0,15,1000);
    DeltaV = V(1,1);
    FragV = V(2,1);

    Emain = 0.5*((totalvolume-
fragvolume)*rho+Mequip)*DeltaV^2;
    Efrag = 0.5*(fragvolume*rho)*DeltaV^2;

end
```

TestDV.m

Determines predicted ΔV for varying depth test cases in Matlab 2015

```
clear
close all
clc

% Chosen test block constants
s = .2032;
Efract = 100;
rho = 1800;

% Test apparatus mass
Mequip = 2.97;

% Explosive energy
expmax = 0.88*5810;

dstep = 0.5;
d = [0.5:dstep:3].*0.0254;

for i = 1:length(d)
    [V(i),~,E(i),~] =
testsplitter(s,d(i),0.0001,expmax,Efract,rho,Mequip);
end


scatter([0,d]./0.0254,[0,V])
xlabel('Borehole Depth (in)');
ylabel('Main Body Velocity (m/s)');
title('Effect of Borehole Depth on Velocity')
```

APPENDIX C.

CALCULATION OF PENDULUM CENTER OF MASS

Shaft						
Length (m)	Diameter (m)	Thickness (m)	CoM	Volume (m^3)	Density (kg/m^3)	Mass (kg)
0.84455	0.01905	0.0015875	0.422275	9.36495E-05	7850	0.735149
Box Top						
Length (m)	Width (m)	Thickness (m)	CoM	Volume (m^3)	Density (kg/m^3)	
0.2286	0.2286	0.0015875	0.84455	8.29595E-05	7850	0.651232
Box Sides						
Length (m)	Width (m)	Thickness (m)	CoM	Volume (m^3)	Density (kg/m^3)	
0.2286	0.2286	0.0015875	0.95885	8.29595E-05	7850	0.651232
Box Bottom						
Length (m)	Width (m)	Thickness (m)	CoM	Volume (m^3)	Density (kg/m^3)	
0.2286	0.2286	0.0015875	1.07315	8.29595E-05	7850	0.651232
Block						
Length (m)	Width (m)	Height (m)	CoM	Volume (m^3)	Density (kg/m^3)	
0.2032	0.2032	0.2032	0.97155	0.008390177	1800	15.10232
Reinforcement						
Width (m)	Length (m)	Thickness (m)	CoM	Volume (m^3)	Density (kg/m^3)	
0.2286	0.0508	0.003175	0.84455	3.68709E-05	7850	0.289437
				Total Mass (kg)		
				18.08059985		
				Center of Mass (m)		
				0.945811409		

APPENDIX D.
FULL LIST OF EXPERIMENTAL RESULTS

Trial #	Drill Depth (in)	Metered Angle (°)	Photoanalysis Angle (°)	Velocity Metered (m/s)	Velocity Photoanalysis (m/s)
1	0	2	2.31	0.106322	0.122728
2	0.5	2.5	3.08	0.132898	0.163664
3	1	3.5	4.62	0.186044	0.245607
4	1.5	4.25	5.39	0.225893	0.286626
5	2	7	7.72	0.371914	0.409941
6	0	2	2.46	0.106322	0.130914
7	0.5	3	3.85	0.159472	0.204621
8	1	3.25	4.00	0.172758	0.212816
9	1.5	5.1	6.17	0.271045	0.327684
10	0	2.5	3.08	0.132898	0.163664
11	0.5	3	3.85	0.159472	0.204621
12	1	3.25	4.00	0.172758	0.212816
13	1.5	4.75	5.39	0.252455	0.286626
14	0	2.25	2.31	0.11961	0.122728
15	0.5	3	3.85	0.159472	0.204621
16	1	3.25	4.00	0.172758	0.212816
17	1.5	5.5	6.94	0.292287	0.368787
18	0	2.25	3.08	0.11961	0.163664
19	0.5	3	3.85	0.159472	0.204621
20	1	3.5	4.62	0.186044	0.245607
21	1.5	4	5.39	0.212611	0.286626
22	0	2.5	3.08	0.132898	0.163664
23	0.5	3	3.85	0.159472	0.204621
24	1	3.5	4.62	0.186044	0.245607
25	1.5	5	6.17	0.265734	0.327684
26	2	5.75	7.72	0.305562	0.409941
27	2	5	6.94	0.265734	0.368787
28	2	5.5	6.94	0.292287	0.368787

29	2	6.5	8.49	0.345378	0.451152
30	2	5.75	7.72	0.305562	0.409941

BIBLIOGRAPHY

[1] Cole, D., and Cox, D. (1964). *Islands in Space.* Philadelphia: Chilton.

[2] Alvarez, L. W., Alvarez, W., Asaro, F., and Michel, H. V. (1980). Extraterrestrial cause for the Cretaceous–Tertiary extinction. *Science* **208(4448)**: 1095–1108. doi:10.1126/science.208.4448.1095.

[3] Morrison, D., (1992), The Spaceguard Survey: Report of the NASA International Near-Earth-Object Detection Workshop. NASA, Washington, D.C.

[4] Canavan, G. H., Solem, J. C., and Rather, D. G. (1993). Proceedings of the Near-Earth-Object Interception Workshop, January 14-16, 1992, Los Alamos, NM. *Los Alamos National Laboratory LA--12476-C.*

[5] Shoemaker, E.M., (1995). Report of the Near-Earth Objects Survey Working Group. NASA Office of Space Science, Solar System Exploration Office.

[6] Ahrens, T. J. and Harris A. W. (1992). Extraterrestrial cause for the Cretaceous–Tertiary extinction. *Nature* **208**: 429–433.

[7] Lu, Edward T.; Love, Stanley G. (2005). Gravitational Tractor For Towing Asteroids. *Nature* **438**: 177–178. doi:10.1038/438177a.

[8] Bombardelli, C. and Peláez, J. (2011). Ion Beam Shepherd for Asteroid Deflection. *Journal of Guidance, Control, and Dynamics*, **34(4)**: 1270–1272

[9] Near-Earth Object Survey and Deflection Analysis of Alternatives Report to Congress March 2007. Retrieved October 27, 2016 from http://neo.jpl.nasa.gov/neo/report2007.html.

[10] Wagner, S., Wie, B., and Barbee, B. (2014). Target selection for a hypervelocity asteroid intercept vehicle flight validation mission. *Acta Astronautica.* **107**: 247-261.

[11] Griffith, A. A. (1921). The phenomena of rupture and flow in solids. *Philosophical Transactions of the Royal Society of London*, A **221**: 163–198, doi:10.1098/rsta.1921.0006.

[12] Irwin, G. (1957). Analysis of stresses and strains near the end of a crack traversing a plate. *Journal of Applied Mechanics* **24**: 361–364.

[13] Kimberly, J. and Ramesh, K. T. (2011). The dynamic strength of an ordinary chondrite. Meteoritics & Planetary Science **46(11)**: 1653–1669. doi: 10.1111/j.1945-5100.2011.01254.

[14] Rivkin, A. (2006). An introduction to near-Earth objects. *Johns Hopkins APL Technical Digest* **27(2)**: 111-120.

[15] Burbine et al. (2002). Meteoritic parent bodies: Their number and identification. In *Asteroids III* (W. F. Bottke Jr. et al., eds.). University of Arizona Press. 653-667.

[16] Britt, D. and Consolmagno, G. (2003). Stony meteorite porosities and densities: a review of the data through 2001. *Meteoritics & Planetary Science,* **38(8)**: 1161-1180.

VITA

James Andrew Veerkamp was born in Missouri City, TX. He attended primary school in Sugar Land, TX. His secondary education was also completed in Sugar Land, where he graduated in 2009. After that, he attended the Missouri University of Science and Technology and received his Bachelor of Science degree in Aerospace Engineering in May 2013. Then, he enrolled there as a graduate student and received his Master of Sccience degree in Aerospace Engineering in December 2016.